The Astrophysical Journal, 935:50 (12pp), 2022 August 10 https://doi.org/10.3847/1538-4357/ac7c6d

Young, Blue, and Isolated Stellar Systems in the Virgo Cluster. I. 2D Optical Spectroscopy

Michele Bellazzini[1], Laura Magrini[2], Michael G. Jones[3], David J. Sand[3], Giacomo Beccari[4], Giovanni Cresci[2], Kristine Spekkens[5,6], Ananthan Karunakaran[6,7], Elizabeth A. K. Adams[8,9], Dennis Zaritsky[3], Giuseppina Battaglia[10,11], Anil Seth[12], John M. Cannon[13], Jackson Fuson[13], John L. Inoue[13], Burçin Mutlu-Pakdil[14,15], Puragra Guhathakurta[16], Ricardo R. Muñoz[17], Paul Bennet[18], Denija Crnojević[19], Nelson Caldwell[20], Jay Strader[21], and Elisa Toloba[22]

[1] INAF â Osservatorio di Astrofisica e Scienza dello Spazio di Bologna, Via Gobetti 93/3, I-40129 Bologna, Italy; michele.bellazzini@inaf.it
[2] INAF—Osservatorio Astrofisico di Arcetri, Largo E. Fermi 5, I-50125 Firenze, Italy
[3] Steward Observatory, University of Arizona, 933 North Cherry Avenue, Rm. N204, Tucson, AZ 85721-0065, USA
[4] European Southern Observatory, Karl-Schwarzschild-Straße 2, D-85748 Garching bei München, Germany
[5] Department of Physics and Space Science, Royal Military College of Canada P.O. Box 17000, Station Forces Kingston, ON K7K 7B4, Canada
[6] Department of Physics, Engineering Physics and Astronomy, Queens University, Kingston, ON K7L 3N6, Canada
[7] Instituto de Astrofísica de Andalucía (CSIC), Glorieta de la Astronomía, E-18008 Granada, Spain
[8] ASTRON, Netherlands Institute for Radio Astronomy, Oude Hoogeveensedijk 4, 7991 PD Dwingeloo, The Netherlands
[9] Kapteyn Astronomical Institute, University of Groningen, PO Box 800, 9700 AV Groningen, The Netherlands
[10] Instituto de Astrofísica de Canarias, Vía Láctea s/n E-38205 La Laguna, Spain
[11] Department of Astrophysics, University of La Laguna, San Cristóbal de La Laguna, E-38206, Spain
[12] Department of Physics & Astronomy, University of Utah, Salt Lake City, UT, 84112, USA
[13] Department of Physics & Astronomy, Macalester College, 1600 Grand Avenue, Saint Paul, MN 55105, USA
[14] Kavli Institute for Cosmological Physics, University of Chicago, Chicago, IL 60637, USA
[15] Department of Astronomy and Astrophysics, University of Chicago, Chicago IL 60637, USA
[16] UCO/Lick Observatory, University of California Santa Cruz, 1156 High Street, Santa Cruz, CA 95064, USA
[17] Departamento de Astronomía, Universidad de Chile, Camino El Observatorio 1515, Las Condes, Santiago, Chile
[18] Space Telescope Science Institute, 3700 San Martin Drive, Baltimore, MD 21218, USA
[19] University of Tampa, 401 West Kennedy Boulevard, Tampa, FL 33606, USA
[20] Center for Astrophysics, Harvard & Smithsonian, 60 Garden Street, Cambridge, MA 02138, USA
[21] Center for Data Intensive and Time Domain Astronomy, Department of Physics and Astronomy, Michigan State University, East Lansing, MI 48824, USA
[22] Department of Physics, University of the Pacific, 3601 Pacific Avenue, Stockton, CA 95211, USA

Received 2022 May 3; revised 2022 June 16; accepted 2022 June 24; published 2022 August 16

Abstract

We use panoramic optical spectroscopy obtained with the Very Large Telescope/MUSE to investigate the nature of five candidate extremely isolated low-mass star-forming regions (Blue Candidates; hereafter, BCs) toward the Virgo cluster of galaxies. Four of the five (BC1, BC3, BC4, and BC5) are found to host several H II regions and to have radial velocities fully compatible with being part of the Virgo cluster. All the confirmed candidates have mean metallicity significantly in excess of that expected from their stellar mass, indicating that they originated from gas stripped from larger galaxies. In summary, these four candidates share the properties of the prototype system SECCO 1, suggesting the possible emergence of a new class of stellar systems, intimately linked to the complex duty cycle of gas within clusters of galaxies. A thorough discussion of the nature and evolution of these objects is presented in a companion paper, where the results obtained here from the MUSE data are complemented with Hubble Space Telescope (optical) and Very Large Array (HI) observations.

Unified Astronomy Thesaurus concepts: Star forming regions (1565); Virgo Cluster (1772); Intracluster medium (858); Low surface brightness galaxies (940); Ram pressure stripped tails (2126); Tidal tails (1701); Galaxy interactions (600)

1. Introduction

The publication of the catalogs of compact HI sources from the ALFALFA (Adams et al. 2013) and GALFA (Saul et al. 2012) surveys triggered observational campaigns aimed at detecting their stellar counterparts, in search of new very dark local dwarf galaxies hypothesized to be associated with the gas clouds (Bellazzini et al. 2015a; Sand et al. 2015; Tollerud et al. 2015). The new experiments failed to find a significant population of such objects (see, e.g., Beccari et al. 2016), but a few new interesting stellar systems were still identified (see, e.g., Giovanelli et al. 2013; Cannon et al. 2015; McQuinn et al. 2015; Tollerud et al. 2015; Bennet et al. 2022).

One of the most curious cases is SECCO 1 (also known as AGC 226067; Adams et al. 2015; Bellazzini et al. 2015a, 2015b; Sand et al. 2015), a low-mass ($M_\star \simeq 10^5\,M_\odot$, $M_{\rm HI} \simeq 2\times10^7\,M_\odot$) star-forming stellar system lying within the Virgo cluster of galaxies. Given the very low stellar mass, the high mean metallicity ($\langle 12+\log({\rm O/H})\rangle = 8.38 \pm 0.11$) implies that the gas fueling the star formation in SECCO 1 was stripped from a relatively massive gas-rich galaxy (Beccari et al. 2017; Sand et al. 2017; Bellazzini et al. 2018), either by a tidal interaction or by ram pressure exerted by the hot intracluster medium (ICM). Indeed, star formation is known to occur in gas clouds stripped from galaxies via both channels (see, e.g., Poggianti et al. 2019; Pasha et al. 2021, and references therein).

Table 1
MUSE Fields

Name	R. A. $_{\rm J2000}$	Decl. $_{\rm J2000}$	Date Obs.	$t_{\rm exp}$	FWHM[a]
BC1	189.756116	12.20542	2018-05-17	966 s × 6	0.″3
BC2	191.114323	12.61824	2018-05-19	966 s × 6	0.″5
BC3	191.677299	10.36919	2019-02-27	966 s × 6	1.″1
BC4L	186.608125	14.38914	2019-02-28	966 s × 6	0.″8
BC4R	186.591389	14.39417	2019-02-28	966 s × 6	0.″5
BC5	186.63014	15.1745	2019-02-10	966 s × 6	0.″5

Note.
[a] The FWHM of the seeing as recorded into the header of the data cubes.

However, in both cases, the star-forming stripped knots are always seen in proximity to the parent galaxy and/or connected to the parent galaxy, either by tidal tails or by the jellyfish structures that are the classical fingerprint of ram pressure stripping (see, e.g., Gerhard et al. 2002; Fumagalli et al. 2011; Yoshida et al. 2012; Fumagalli et al. 2014; Kenney et al. 2014; Fossati et al. 2016; Bellazzini et al. 2019; Nidever et al. 2019; Corbelli et al. 2021a, 2021b). In contrast, SECCO 1 is extremely isolated, lying more than 200 kpc, in projection, from the nearest candidate parent galaxy (Sand et al. 2017; Bellazzini et al. 2018; Jones et al. 2022a).

Simple theoretical arguments (Burkhart & Loeb 2016), as well as dedicated hydrodynamical simulations (Bellazzini et al. 2018; Calura et al. 2020), suggest that gas clouds similar to SECCO 1 may survive as long as $\sim$1 Gyr within clusters of galaxies, kept together by the pressure confinement of the ICM, thus leaving room for very long voyages from the site of origin. Star formation is also expected to occur in the meantime (Kapferer et al. 2009; Calura et al. 2020). If cloudlets such as these are indeed able to survive for such long times and form stars, a rich population of them should be among the inhabitants of galaxy clusters, given the complex processes in which the gas is involved in these environments (Poggianti et al. 2019; Boselli et al. 2022).

Prompted by these considerations, a search for similar systems in the Virgo cluster was performed (see Sand et al. 2017; Jones et al. 2022b), and a sample of five Blue Candidates (BCs) was selected from UV and optical images, as described in Jones et al. (2022a). To confirm the nature of these BCs, spectroscopic follow-up is essential, to: (a) measure their radial velocity (RV) and confirm their location within the Virgo Cluster; (b) quantify any ongoing star formation, by detecting and analyzing the associated H II regions; and (c) estimate the metallicity of the gas in the star-forming regions, a crucial diagnostic for assessing the origin of these systems.

Here, we present the results of Very Large Telescope (VLT)/Multi Unit Spectroscopic Explorer (MUSE; Bacon et al. 2014) observations of five such BC stellar systems, fully analogous to the study by Beccari et al. (2017; hereafter, Be17) for SECCO 1. Four of them are confirmed as likely residing in Virgo and similar to SECCO 1. Individual H II regions are identified, velocities and line fluxes are measured from their spectra, and metallicity estimates are provided. Finally, their chemical and kinematic properties are briefly discussed. In a companion paper (paper II; Jones et al. 2022a; hereafter, Pap-II), Hubble Space Telescope (HST) imaging and photometry, as well as new Very Large Array and Green Bank telescope HI observations for the BCs are presented. Pap-II also discusses the nature and origin of this potentially new class of stellar systems, based on the entire set of available observations. A more detailed discussion of BC3, also known as AGC 226178, the only system that has been the subject of previous analyses (Cannon et al. 2015; Junais et al. 2021), has been presented by Jones et al. (2022b).

2. Observations and Data Reduction

Integral field unit optical (4650–9300 Å) spectroscopy of six 1.′0 × 1.′0 fields centered on the targets was acquired with MUSE (Bacon et al. 2014), mounted at the Unit 4 (Yepun) VLT, at ESO, Paranal (Chile), as part of program 0101.B-0376A (P.I: R. Munõz). The spectral resolution is in the range $\frac{\lambda}{\Delta\lambda} \simeq 2000$–4000, from the bluest to the reddest wavelength. Two partially overlapping MUSE pointings were required to sample all the sources presumably associated with BC4. We refer to these two fields and portions of the BC4 system as BC4L (left) and BC4R (right), with BC4L lying to the east-southeast of BC4R. For each field, six $t_{\rm exp} = 966$ s exposures were acquired, with a dithering scheme based on regular derotator offsets, to improve the flat-fielding and homogeneity of the image quality across the field. The observing log is presented in Table 1. Each set of raw data was wavelength- and flux-calibrated, then stacked into a single, final data cube per field, using the MUSE pipeline (Weilbacher et al. 2012).

The spectra of the sources associated with each candidate were visually inspected using SAOimage DS9, looking for Hα emission in the redshift range compatible with membership of the Virgo cluster (-500 km s$^{-1} \lesssim cz \lesssim 3000$ km s^{-1}; Mei et al. 2007). This was easily found in all the sources, except BC2. As discussed in Pap-II, BC2 appears to be a small group of background blue galaxies in the HST imaging, mimicking the appearance of the other BC objects in our sample. This, combined with the lack of Hα emission, led us to dismiss it as a spurious candidate and not analyze it further. As in Pap-II, we adopt for all our targets the distance to the Virgo cluster of Mei et al. (2007), $D = 16.5$ Mpc.

For the detection of the individual sources within each field, and to extract their spectra, we adopted the same approach as Be17. In particular, for each stacked data cube we proceeded as follows.

1. The data cube was split into 3801 single layers, sampling the targets from 4600.29 to 9350.29 Å, with a step in wavelength of 1.25 Å.
2. An Hα image was produced by stacking together the four layers where the local Hα signal reached its maximum,

Table 2
Position, RV, and Observed Hα Flux of the Individual Sources

Name	R.A. (deg)	Decl. (deg)	RV (km s^{-1})	ϵRV (km s^{-1})	$N_{\rm RV}$	F(Hα) (10^{-18} erg cm^{-2} s^{-1})	ϵF(Hα) (10^{-18} erg cm^{-2} s^{-1})	FWHM arcsec
BC1s11	189.75810	12.20365	1111.3	5.5	7	97.6	7.9	2.2
BC1s12	189.75754	12.20245	1113.4	6.3	5	58.8	5.9	8.2
BC1s13	189.76160	12.20350	1117.3	7.3	5	69.0	6.5	2.4
BC1s14	189.75489	12.20448	1120.8	10.8	4	23.4	4.2	1.5
BC1s15	189.75585	12.20327	1109.1	8.1	5	49.6	5.5	3.6
BC1s17	189.75859	12.20172	1119.7	5.6	4	14.1	3.7	1.2
BC1s20	189.75723	12.20065	1119.0	9.5	5	40.8	5.0	2.9
BC1s57W[a]	189.75637	12.20567	1126.9	20.0	1	9.4	3.0	1.3
BC1s61W[a]	189.75583	12.20534	1120.9	20.0	1	8.6	3.0	0.5
BC1s62W[a]	189.75534	12.20506	1115.4	20.0	1	8.4	3.4	0.6
BC1s65W[a]	189.76471	12.20468	1124.0	13.0	3	11.7	3.6	1.7
BC1s67W[a]	189.75644	12.20414	1102.0	23.4	2	8.3	3.4	1.5
BC1s73W	189.75604	12.20332	1108.0	5.2	5	43.6	5.2	2.6
BC1s80W	189.75777	12.20287	1115.5	2.0	4	57.4	5.9	4.0
BC1s83W	189.75667	12.20241	1117.3	17.2	4	13.5	3.7	0.9
BC1s90W	189.75751	12.20178	1117.7	6.6	4	55.0	5.8	1.7
BC1s92W	189.75840	12.20138	1121.9	20.0	1	15.3	3.8	0.5
BC1s98W	189.75757	12.20055	1124.6	15.1	4	29.5	4.5	1.4
BC3s4	191.67637	10.37416	1575.7	7.2	5	219.7	14.0	5.3
BC3s9	191.67924	10.37005	1587.4	9.9	4	167.2	11.4	2.7
BC3s10	191.67892	10.36901	1582.6	5.3	7	465.3	26.3	1.9
BC3s12	191.67594	10.36945	1586.0	8.5	4	33.4	4.7	2.4
BC3s13	191.67792	10.36832	1582.5	7.4	5	62.6	6.1	1.7
BC3s14	191.67730	10.36820	1578.7	6.2	3	24.9	4.2	1.5
BC3s15	191.67549	10.36701	1583.7	5.8	7	390.4	22.5	3.6
BC3s16	191.67691	10.36682	1583.7	5.8	7	63.1	6.2	4.3
BC3s18	191.67344	10.36558	1583.7	5.8	7	489.6	27.5	1.6
BC3s19	191.68198	10.36358	1582.5	8.3	5	68.4	6.4	5.2
BC3s20	191.68117	10.36314	1582.5	8.3	5	53.0	5.7	3.3
BC3s23	191.67339	10.36230	1583.6	20.0	1	12.5	3.6	0.7
BC3s24W	191.67529	10.37407	1583.6	20.0	1	27.4	4.4	1.4
BC3s26W	191.67561	10.37388	1584.1	5.8	4	49.6	5.5	1.2
BC3s69W	191.67186	10.36344	1595.6	20.0	1	12.5	3.5	1.1
BC4s3L	186.60278	14.39644	−55.7	7.1	5	10.7	3.5	1.1
BC4s4L	186.60263	14.39481	−59.4	1.1	5	121.9	9.1	1.2
BC4s8L	186.60766	14.38708	−78.3	1.7	7	143.3	10.2	1.2
BC4s9L	186.60658	14.38645	−82.6	1.3	6	89.0	7.4	1.8
BC4s10L	186.60584	14.38589	−85.2	1.6	6	149.8	10.5	2.6
BC4s11L	186.61344	14.38647	−46.5	1.8	6	49.8	5.5	1.5
BC4s12L	186.61272	14.38597	−49.3	3.9	6	44.9	5.2	4.2
BC4s13L	186.60643	14.38496	−81.4	4.9	3	6.7	3.3	1.2
BC4s14L	186.60498	14.38439	−81.3	2.0	3	17.8	3.9	2.1
BC4s38WL	186.60586	14.38522	−83.6	4.6	5	19.7	4.0	1.6
BC4s11R	186.58587	14.39747	−33.4	5.2	5	8.1	3.4	0.9
BC4s12R	186.59377	14.39739	−47.6	15.0	3	11.4	3.6	0.9
BC4s15R	186.59044	14.39478	−46.4	1.3	6	67.7	6.4	2.8
BC4s34WR	186.59354	14.39690	−54.4	7.3	2	4.8	3.2	1.5
BC4s40WR	186.58970	14.39530	−41.6	4.3	5	8.9	3.4	0.8
BC4s41WR	186.59118	14.39515	−27.1	13.6	2	8.4	3.4	1.3
BC5s3[b]	186.63569	15.16547	−64.4	20.0	1	39.7	5.0	.1.1
BC5s9	186.62805	15.17529	−78.2	4.1	5	111.7	8.6	2.9
BC5s10	186.62818	15.17447	−76.8	11.1	5	73.0	6.6	1.4
BC5s12	186.62856	15.17307	−75.8	9.2	6	213.0	13.7	4.1

Notes. Column descriptions: name of the source; R.A. (J2000); decl. (J2000); heliocentric RV and its uncertainty (ϵRV); Hα flux and its uncertainty (ϵF(Hα)); and the FWHM as measured by `Sextractor`.

[a] These sources may be particularly affected by contamination from the diffuse emission associated with BC1.

[b] Source located at the edge of the field of view, only partially included in the data cube. The missing numbers in the nomenclature of the individual sources (like, e.g., BC1s1 to BC1s10 or BC3s5 to BC3s8) correspond to sources that were detected by `Sextractor` but did not pass the selection by visual inspection of the spectra described in Section 2. F(Hα) is the observed flux, not corrected for extinction (see Table 3).

Table 3
Line Fluxes of the Individual Sources, in Units of the Hβ Flux, Set to F(Hβ) = 100

Name	F(Hβ) (10^{-18} erg cm^{-2} s^{-1})	[O III]$_{5007}$	Hα	[N II]$_{6584}$	[S II]$_{6717}$	[S II]$_{6731}$	C$_\beta$ mag
BC1s11	8.1 ± 3.4	138.3 ± 45.2	299.4 ± 97.2	24.3 ± 42.0	49.8 ± 48.0	34.7 ± 44.7	1.99 ± 0.21
BC1s12	13.6 ± 3.7	⋯	290.5 ± 43.7	23.1 ± 23.8	73.1 ± 27.7	49.6 ± 25.9	0.57 ± 0.16
BC1s13	21.8 ± 4.1	⋯	287.8 ± 29.6	19.0 ± 14.8	94.1 ± 19.0	61.6 ± 17.2	0.14 ± 0.12
BC1s14	6.9 ± 3.3	⋯	288.4 ± 60.3	37.5 ± 45.5	91.0 ± 48.7	51.8 ± 46.4	0.23 ± 0.28
BC1s15	11.9 ± 3.6	⋯	290.2 ± 46.0	17.2 ± 26.4	103.9 ± 32.8	76.5 ± 30.8	0.52 ± 0.18
BC1s17	4.0 ± 3.2	⋯	288.8 ± 92.8	⋯	⋯	⋯	0.29 ± 0.46
BC1s20	13.1 ± 3.7	⋯	287.7 ± 38.4	19.0 ± 23.8	66.1 ± 26.4	45.7 ± 25.3	0.11 ± 0.17
BC1s62W	6.4 ± 3.3	⋯	131.1 ± 53.5	⋯	⋯	⋯	0.00 ± 0.40
BC1s73W	7.3 ± 3.4	⋯	293.3 ± 70.8	18.4 ± 42.9	109.6 ± 52.7	68.6 ± 48.4	1.01 ± 0.25
BC1s80W	12.6 ± 3.6	39.4 ± 25.9	291.0 ± 46.6	22.1 ± 25.6	65.4 ± 29.1	42.6 ± 27.3	0.64 ± 0.17
BC1s83W	3.7 ± 3.2	⋯	288.9 ± 98.0	10.0 ± 80.7	170.1 ± 90.8	93.3 ± 86.0	0.31 ± 0.48
BC1s90W	12.3 ± 3.6	⋯	290.8 ± 46.7	12.3 ± 25.3	80.5 ± 30.7	58.1 ± 29.0	0.61 ± 0.17
BC1s92W	5.0 ± 3.2	⋯	287.6 ± 75.3	33.7 ± 61.7	42.9 ± 62.2	34.2 ± 61.8	0.09 ± 0.38
BC1s98W	12.3 ± 3.6	⋯	239.8 ± 36.4	12.3 ± 25.0	66.0 ± 27.7	40.1 ± 26.4	0.00 ± 0.19
BC3s4	70.3 ± 6.5	⋯	287.7 ± 19.9	10.8 ± 4.8	52.1 ± 7.1	34.8 ± 6.2	0.12 ± 0.07
BC3s9	49.6 ± 5.5	14.7 ± 6.8	288.4 ± 22.9	12.3 ± 6.8	33.2 ± 8.0	19.6 ± 7.2	0.22 ± 0.08
BC3s10	143.1 ± 10.1	37.1 ± 4.0	288.1 ± 18.3	12.8 ± 2.8	27.4 ± 3.7	20.3 ± 3.2	0.17 ± 0.05
BC3s12	6.9 ± 3.3	⋯	291.5 ± 67.7	⋯	⋯	⋯	0.73 ± 0.27
BC3s13	13.4 ± 3.7	⋯	291.1 ± 45.6	16.6 ± 23.6	32.4 ± 25.0	22.7 ± 24.2	0.67 ± 0.16
BC3s15	124.8 ± 9.2	195.1 ± 12.3	287.7 ± 18.0	9.5 ± 2.9	23.0 ± 3.7	19.2 ± 3.4	0.12 ± 0.06
BC3s16	13.8 ± 3.7	48.4 ± 24.2	291.0 ± 44.5	23.2 ± 23.5	51.7 ± 25.9	36.7 ± 24.7	0.64 ± 0.16
BC3s18	47.5 ± 5.4	⋯	298.1 ± 57.9	10.5 ± 8.1	24.4 ± 10.9	16.7 ± 9.5	1.77 ± 0.07
BC3s19	24.9 ± 4.2	⋯	274.8 ± 25.8	15.8 ± 12.8	34.2 ± 13.8	24.7 ± 13.3	0.00 ± 0.11
BC3s20	8.7 ± 3.4	⋯	293.4 ± 64.7	1.8 ± 34.5	44.8 ± 39.2	25.3 ± 37.1	1.04 ± 0.21
BC3s26W	14.4 ± 3.7	44.1 ± 23.0	288.5 ± 37.9	15.9 ± 21.7	47.7 ± 23.6	51.7 ± 23.9	0.25 ± 0.16
BC4s4L	31.0 ± 4.6	15.4 ± 10.5	289.7 ± 29.3	108.4 ± 17.0	31.9 ± 11.9	21.9 ± 11.2	0.43 ± 0.09
BC4s8L	38.6 ± 4.9	46.6 ± 10.2	289.3 ± 26.3	109.5 ± 14.8	33.5 ± 10.0	24.4 ± 9.4	0.36 ± 0.08
BC4s9L	20.9 ± 4.0	23.5 ± 15.6	290.5 ± 35.6	104.0 ± 22.0	39.8 ± 17.3	28.2 ± 16.5	0.54 ± 0.12
BC4s10L	39.0 ± 4.9	5.9 ± 8.0	289.6 ± 26.9	103.5 ± 14.6	27.6 ± 9.6	33.3 ± 10.0	0.40 ± 0.08
BC4s11L	9.8 ± 3.5	111.7 ± 36.5	292.0 ± 55.9	152.1 ± 43.8	53.4 ± 35.4	33.0 ± 33.5	0.79 ± 0.20
BC4s12L	12.0 ± 3.6	41.6 ± 27.1	289.3 ± 43.7	142.6 ± 34.2	81.3 ± 30.3	51.4 ± 28.4	0.37 ± 0.18
BC4s14L	5.7 ± 3.3	⋯	287.8 ± 68.8	44.6 ± 55.5	28.6 ± 54.6	19.8 ± 54.1	0.13 ± 0.34
BC4s38WL	4.2 ± 3.2	⋯	291.3 ± 94.2	91.9 ± 78.3	60.3 ± 75.7	35.2 ± 73.8	0.67 ± 0.41
BC4s15R	17.3 ± 3.9	⋯	289.7 ± 36.9	85.6 ± 23.1	38.1 ± 19.9	19.1 ± 35.0	0.43 ± 0.14
BC5s9	29.4 ± 4.5	16.4 ± 11.0	289.4 ± 29.2	69.9 ± 14.8	39.3 ± 12.8	26.3 ± 12.0	0.39 ± 0.10
BC5s10	18.2 ± 3.9	⋯	289.9 ± 36.6	23.7 ± 18.1	91.4 ± 23.0	60.5 ± 20.79	0.46 ± 0.13
BC5s12	56.7 ± 5.8	9.4 ± 5.8	289.3 ± 24.1	77.7 ± 10.3	46.2 ± 8.3	29.5 ± 7.24	0.37 ± 0.07

Note. F(Hβ) is the observed flux, while all other (normalized) line fluxes are corrected for extinction C_β.

corresponding to a spectral window of 5.0 Å, and a white image was produced by stacking together all 3801 layers.

3. Both images were searched for sources with intensity peaks above 3.0σ from the background level, using the photometry and image analysis package `Sextractor` (Bertin & Arnouts 1996). The two lists of detected sources were then merged together into a single master list.
4. Photometry through an aperture of radius $1\farcs5$ was performed with `Sextractor` on each individual-layer image for all the sources included in the master list.
5. The fluxes measured in each layer were then recombined, obtaining a 1D spectrum for each source.
6. Finally, the spectra of all the measured sources were visually inspected, and only those having clear emission at least in Hα were retained in the final catalog, which is presented in Table 2. Sources that were originally detected only in the white-light image are denoted by the W at the ends of their names.

We identify emission lines across the MUSE spectral range, including Hβ, [O III]4959, [O III]5007, [N II]6548, Hα, [N II] 6583, [S II]6717, and [S II]6731. The heliocentric RV of each of the 53 sources included in the final catalog has been measured by fitting all the identified emission lines with a Gaussian curve to estimate their centroid and, consequently, the shift with respect to their rest wavelength, with the IRAF task RVIDLINES. The final RV was derived from the average wavelength shift, while the uncertainty (ϵRV) is the associated rms divided by the square root of the number of lines involved in the estimate ($N_{\rm RV}$). Based on the scatter between the velocities of different lines for the same source, an uncertainty of 20.0 km s^{-1} was adopted for the sources whose RV has been estimated from one single line (Hα). The positions, RVs (and associated uncertainties), Hα fluxes (and associated uncertainties), and FWHMs of all the identified sources are listed in Table 2.

It is possible that the spectra of some of the sources detected in white light are a combination of an emission component (coming from the diffuse hot gas associated with the BC) superimposed on an unrelated background/foreground source (whose flux triggered the detection in white light). We decided to keep these sources in the final list, as, in any case, they provide additional sampling of the velocity fields and the

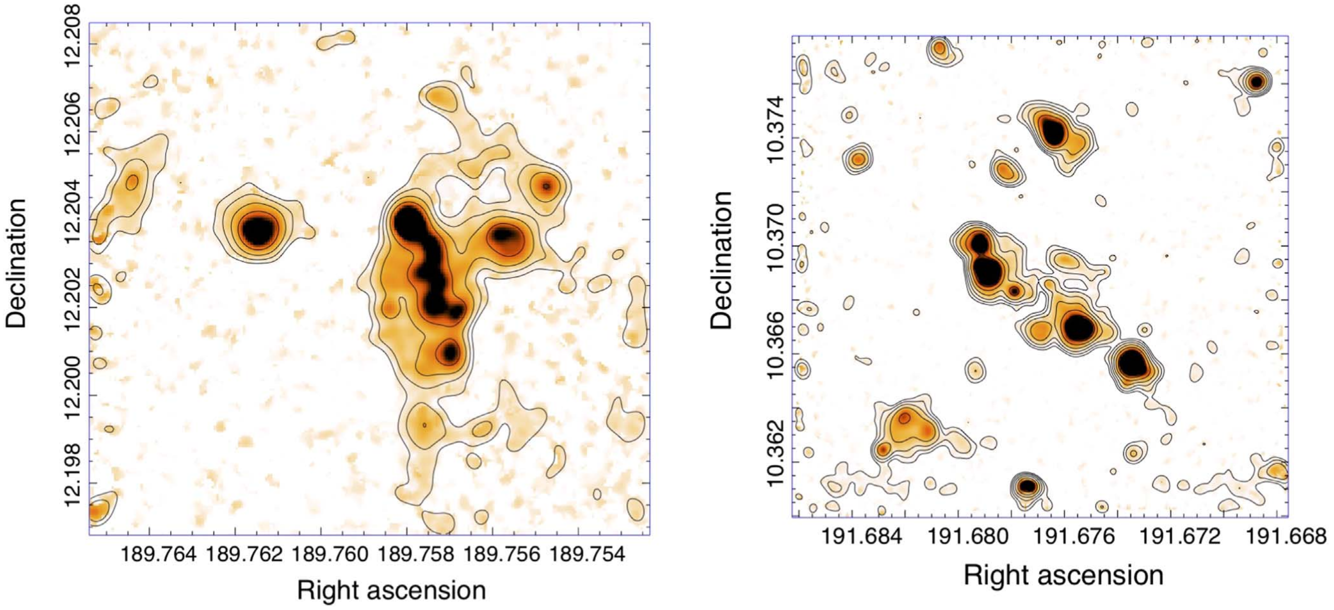

(a) (b)

Figure 1. Maps of the Hα emission from BC1 (a) and BC3 (b). The levels of the contours are at 2, 4, 8, 16, 32, 64, 128, and 256 × 10^{-20} erg cm $^{-2}$ s^{-1}. Right ascension and decl. are in degrees.

oxygen abundance of the considered systems. Several of the sources listed in Table 2 have FWHMs, as measured by `Sextractor`, significantly larger than the seeing (see Table 1), indicating that they are extended. In some cases, the FWHMs are also significantly larger than the aperture that we used to extract the spectra from the data cube. We found that the adopted aperture radius of 1."5 was a reasonable trade-off for maximizing the signal-to-noise ratio (S/N) of the average source, while minimizing the contamination from adjacent sources.

Line fluxes and their associated uncertainties have been obtained with the task SPLOT in IRAF, as done in Be17, and are listed in Table 3, for the subset of 37 sources having valid measures of both the Hα and Hβ fluxes. These allow an estimate of the extinction (C_β, also listed in Table 3), computed from the ratio between the observed and theoretical Balmer decrements for the typical conditions of an H II region (see Osterbrock & Ferland 2006). Within the same complex of H II regions, there can be significant reddening differences. The measured extinction is both that within each H II region and that outside, between the observer and the object (see, e.g., Caplan & Deharveng 1986). Some regions have likely higher internal extinction than others in the same group, such as BC1s11 and BC3s18, the most extincted regions of our sample. Also, within each BC we notice a variation in the degree of ionization among the various H II regions, as evidenced by the observation of [OIII] lines in only some of them. These variations are very similar to those observed in SECCO 1 (Be17), and, as in that case, they do not appear to be associated with metallicity variations, but with the temperature of the ionizing stars (see, e.g., Bellazzini et al. 2018).

The uncertainties in the line fluxes can be very large in some cases, in particular for [NII] and [S II] lines, owing to the low S/N. Still, we preferred to keep these measures, as they may bring useful information for deriving the average properties of the stellar systems.

3. Morphology, Classification, and Kinematics

In Figure 1 and Figure 2 we show the continuum-subtracted Hα images of BC1, BC3, BC4L, BC4R, and BC5, with intensity contours ranging from 2 × 10^{-20} erg cm $^{-2}$ s^{-1} to 256 × 10^{-20} erg cm $^{-2}$ s^{-1}, spaced by a factor of 2. Each image was obtained by subtracting a continuum image from the Hα image described above. The continuum image was created by stacking four slices of the cube near the emission line, in particular from 2.5 to 7.5 Å blueward of the analogous window centered on Hα. In other words, the continuum image has the same wavelength width as the Hα image, but is shifted by ≃7.5 Å to the blue of the Hα line.

All the images display objects whose morphology is very similar to SECCO 1: several compact sources, often distributed in elongated configurations, which are surrounded by diffuse ionized emission. All the systems, except BC5,[23] appear fragmented into separate pieces, with the typical separation ≲0.'5, corresponding to ≲2.4 kpc at the distance of Virgo. The two pieces of BC4 are separated by ~8 kpc, in projection, very similar to the separation between the Main Body and the Secondary Body of SECCO 1 (Sand et al. 2015; Bellazzini et al. 2018). The extension of the different systems is different by a factor of a few. The bright Hα knots of BC1 can be approximately enclosed within a circle of projected radius ≃1.4 kpc; this radius for BC3, BC4L, BC4R, and BC5 is ≃1.8, 2.2, 1.2, and 0.5 kpc, respectively. A deeper insight into the

---

[23] In fact, there is one source, BC5s3, that is only partially imaged by the BC5 data cube, lying at its southern edge. It is located ≃0.'7 apart from the main BC5 clump of sources shown in Figure 2(c). A map of BC5 sources, including BC5s3, is presented in Section 3.

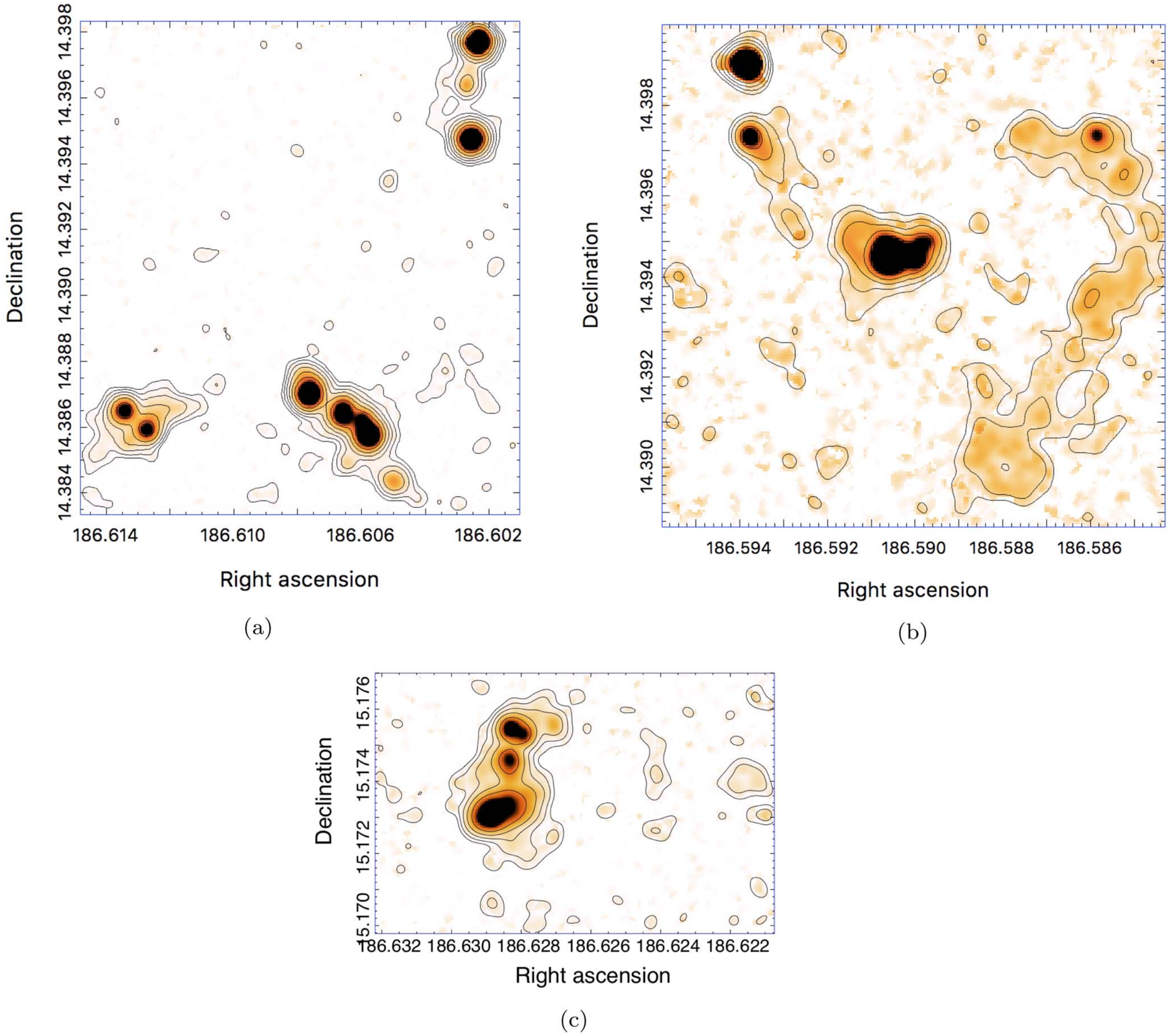

Figure 2. Maps of the Hα emission from BC4L (a), BC4R (b), and BC5 (c). The levels of the contours are at 2, 4, 8, 16, 32, 64, 128, and 256 × 10^{-20} erg cm $^{-2}$ s^{-1}. Right ascension and decl. are in degrees.

morphology of the BCs is presented in Pap-II, based on the inspection of the HST images.

The issue of the classification of the individual sources detected with `Sextractor` is addressed in Figure 3, where three different diagnostic plots based on line ratios are presented for the (different) subsets of the sources having measures of the flux in the involved lines. While the uncertainties are large in some cases, all the considered sources behave as H II regions, the only possible exception being BC2s12L, which lies just within the contour enclosing supernova remnants in the middle panel of Figure 3. We conclude that all the systems are actively forming stars, fully analogous to the case of SECCO 1. In Figure 4, we show the spectra of the sources with the strongest Hα line in each BC, to show the quality of the best spectra in our data set.

Before proceeding with the analysis of the internal kinematics of the new stellar systems, it may be worth putting them in context within the Virgo cluster of galaxies. In Figure 5(a), BC1, BC3, BC4, and BC5, together with SECCO 1, are shown in projection on a wide map of Virgo, as traced by the distribution of galaxies included in the Extended Virgo Cluster Catalog (EVCC; Kim et al. 2014). The main substructures of the cluster are labeled following Boselli et al. (2014). Figure 5(b) shows that all our targets have mean velocities (from Table 5) within the range spanned by the EVCC galaxies, hence they are very likely members of the Virgo cluster, a conclusion that is also supported by the HST data (Pap-II).[24] In particular, BC1 and BC3 are consistent with membership to Cluster C, while SECCO 1, BC4, and BC5 may belong to the Low Velocity Cloud or Cluster A. According to Boselli et al. (2014), all these substructures of Virgo have the same mean distance from us. In the following, we will consider all the newly confirmed BCs and SECCO 1 as members of the Virgo cluster, adopting D = 16.5 Mpc (Mei et al. 2007) for all of them, as done in Pap-II.

---

[24] For example, by resolving the BCs into stars and showing that their color–magnitude diagrams are consistent with a young stellar population at the distance of Virgo (see also Jones et al. 2022b).

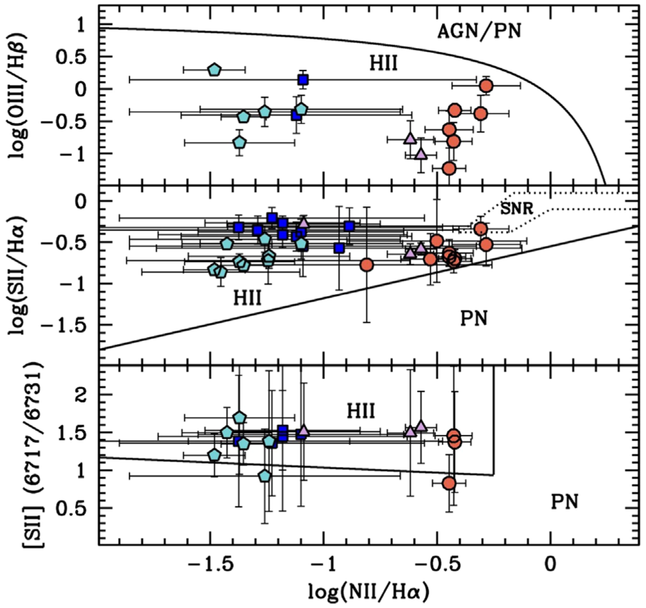

Figure 3. Line-ratio diagnostic diagrams for all the individual sources for which it was possible to measure the relevant line fluxes from MUSE spectra. The symbol coding is as follows: blue squares—BC1; turquoise pentagons—BC3; red circles—BC4; and plum triangles—BC5. The lines separating the different kinds of sources in the diagrams are: upper panel—Equation (5) from Kewley et al. (2001); middle panel—Equation (3) from Kniazev et al. (2008); and lower panel—Equations (4) and (5) from Kniazev et al. (2008). In the middle panel, a dotted line contour encloses the region of the diagram where the supernova remnants (SNR) are expected to lie.

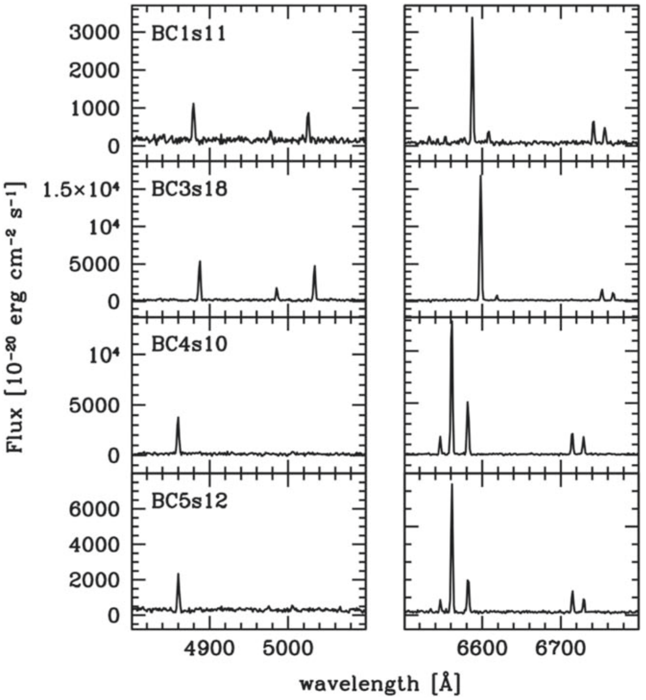

Figure 4. Spectra of the sources with the strongest Hα lines in each BC. For each source, two portions of the MUSE spectra are shown, enclosing the most relevant emission lines: Hβ, [O III]4959, and [O III]5007 (left panels), and [N II]6548, Hα, [N II]6583, and [S II]6717+6731 (right panels).

In Figure 6, the maps of all the individual sources detected with `Sextractor` are shown for all the considered systems, color-coded according to the source RV. BC4L and BC4R are shown on the same map; their proximity and similar RVs indicate their common origin. In each BC, the star-forming sources have the same RVs, within a few tens of km s^{-1}, indicating that all are part of the same system, having a common origin, which is also confirmed by their chemical homogeneity (see Section 4). In all cases, some sign of the kinematic coherence of subgroups of adjacent sources is perceivable, suggesting that the systems are structured into clumps, which, possibly, are slowly flying apart from one another (see below). To make a direct comparison between the physical size and the kinematics of the various systems, including the RV uncertainties, in Figure 7 we plot the projected distance from the center of the system (along the R.A. direction, R.A. offset) and the RV of each individual source. The adopted centers are listed in Table 5. BC4L and BC4R are shown separately (the middle panels of Figure 7) and together in a single panel (the lower left panel). The observed configurations suggest different degrees of spatial and kinematic coherence, with some hints of velocity gradients. In particular, the diagram showing the two pieces of BC4 together may suggest the case of a system moving toward us, led by the dense clump around R.A. offset = −2 kpc, while the sources to both sides of it are lagging behind in proportion to their physical distance, reminiscent of the configuration produced in the simulation with star formation by Calura et al. (2020; see their Figure 11).

The RV distributions displayed in Figure 6 and Figure 7 suggest that a simple velocity dispersion is probably not adequate for capturing the internal kinematics of these systems. The σ values listed in Table 5 are standard deviations, not corrected for observational uncertainties. These are of the order of the uncertainties on the individual RV estimates, suggesting that the velocity dispersions are not resolved by our data. To gain a deeper insight into this problem, we make an attempt to estimate the intrinsic dispersion of the two systems showing both the highest degree of kinematic coherence[25] and the largest number of individual sources, BC1 and BC3. To obtain reliable uncertainties associated with each RV estimate, we selected only sources whose RV and ϵRV were obtained from at least three different spectral lines, thus selecting samples of 13 and 12 sources for BC1 and BC3, respectively.

From these data, we derived the probability density function (PDF) of the parameters of a simple Gaussian model ($V_{\rm sys}$, $\sigma_{\rm int}$), through a Bayesian analysis, using a Monte Carlo Markov Chain (MCMC) analysis, as done in Bellazzini et al. (2019). We used `JAGS`,[26] within the `R`[27] environment, to run four independent MCMCs of 10,000 steps each, after a burn-in phase of 1000 steps. For both parameters, uniform priors were adopted: for $V_{\rm sys}$, in a range of $\simeq\pm50$ km s^{-1} around the mean RV, and for $\sigma_{\rm int}$, in the range $0.0\ {\rm km\ s^{-1}} < \sigma_{\rm int} < 10.0\ {\rm km\ s^{-1}}$. The resulting 2D PDFs, as sampled by the MCMCs, are shown in Figure 8. The median (P_{50}) ± the semi-difference between the 16th and 84th percentiles of the marginalized $V_{\rm sys}$ PDF are $P_{50} = 1115.4 \pm 1.2$ km s^{-1} for BC1 and $P_{50} = 1582.6 \pm 2.1$ km s^{-1} for BC3, in agreement, within the uncertainty, with the straight averages listed in Table 5. On the other hand, Figure 8 clearly demonstrates that the velocity dispersions are unresolved by our data, even in these most favorable cases. For both systems, the PDF reaches its maximum at $\sigma_{\rm int} = 0.0$ km s^{-1}.

---

[25] It is important to recall that the kinematic coherence is observed only in the RV. In principle, velocity gradients similar to those observed in BC4 may also be present in BC1 and BC3, just hidden by projection effects.

[26] http://mcmc-jags.sourceforge.net

[27] https://www.r-project.org

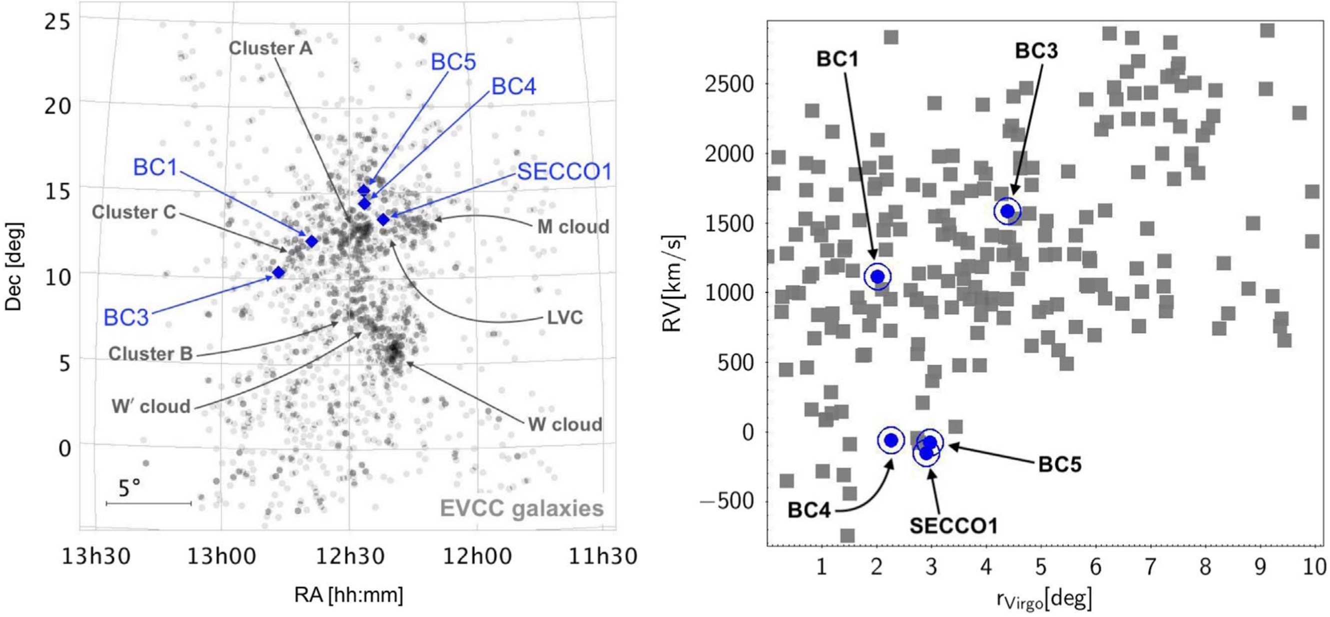

(a) (b)

Figure 5. Locations of the BCs and SECCO 1 within the Virgo cluster. In panel (a), the positions of the systems (blue diamonds) are indicated within a wide map of the Virgo cluster, as traced by the distribution of the EVCC galaxies (small gray circles; Kim et al. 2014); the main substructures of the cluster are labeled following Boselli et al. (2014). In panel (b), the EVCC galaxies (gray squares) and BCs (encircled blue filled circles) are plotted into a phase-space diagram opposing the heliocentric line-of-sight velocity to the angular distance from M 87, taken as the center of the Virgo cluster.

For BC1 (BC3) half of the points sampling the PDF have $\sigma_{\rm int} \leqslant 1.7$ (1.6) km s^{-1}, 75% have $\sigma_{\rm int} \leqslant 3.0$ (2.8) km s^{-1}, and 95% have $\sigma_{\rm int} \leqslant 5.6$ (5.1) km s^{-1}. It can be concluded that BC1 and BC3 may have $\sigma_{\rm int}$ virtually anywhere between $\simeq$0 km s^{-1} and $\simeq$6 km s^{-1}, but most likely $\sigma_{\rm int} \leqslant 3.0$ km s^{-1}.

Calura et al. (2020) introduced a stellar virial ratio ($\alpha_{\rm vir}$; their Equation (8)) as a simple parameter for evaluating whether a stellar system is gravitationally bound ($\alpha_{\rm vir} \lesssim 1$) or not ($\alpha_{\rm vir} \gg 1$). We can use a version of their equation, having the half-light radius (R_h) as an input parameter, instead of the 3D half-mass radius, to estimate $\alpha_{\rm vir}$ for the BCs. Pap-II estimates the stellar masses of these systems as being in the range $4 \times 10^4 M_\odot - 1 \times 10^5 M_\odot$. Assuming, conservatively, $M = 10^5 M_\odot$, taking $R_{\rm med}$ from Table 5 as a proxy for R_h, and adopting $\sigma_{\rm int} = 1.0$ km s^{-1}, we obtain $\alpha_{\rm vir} = 6.9$, 11.7, 7.4, 6.8, and 4.2 for BC1, BC3, BC4L, BC4R, and BC5, respectively. Assuming $\sigma_{\rm int} = 2.0$ km s^{-1} would move all the $\alpha_{\rm vir}$ to values in the range 15–50, while keeping $\sigma_{\rm int} = 1.0$ km s^{-1}, and assuming $M = 10^6 M_\odot$ would imply $\alpha_{\rm vir} \lesssim 1$ for all the systems. We conclude that BC1, BC3, BC4L, BC4R, and BC5 are most likely unbound, as stellar systems. However, they can be considered somewhat borderline, given the sizeable uncertainties in all the parameters involved in the computation of $\alpha_{\rm vir}$ and the inadequacy of a simple Gaussian for modeling their velocity distribution. It is quite possible that some of the subclumps they are made of would leave a bound remnant, a small open cluster-like system floating undisturbed within Virgo, while its stars evolve passively (a hypothesis already suggested by Bellazzini et al. 2018).

4. Metallicity and Star Formation

Given the available lines with measured fluxes, corrected for extinction, we estimated the gas-phase oxygen abundance using two different strong-line ratios, N2=[NII]/Hα and O3N2=([OIII]/Hβ)/([NII]/Hα), as defined by Pettini & Pagel (2004; hereafter, PP04). We were able to measure N2 for the 35 sources listed in Table 4 and O3N2 for 15 of them. In Table 4, we provide the values of 12+log (O/H) derived from N2 and O3N2, using both the calibration by PP04 and by (Marino et al. 2013; hereafter, M13). The individual errors on the oxygen abundance of each region properly include the contribution of the uncertainties on the fluxes of the emission lines and on their correction for reddening, as well as the contribution of the uncertainty associated with the adopted calibrations. Following Be17, to compensate for the effects of varying ionization, we compute the oxygen abundance as the average of the abundances from N2 and O3N2 (N2+03N2), taking the average from the PP04 calibrations as our preferred value. The mean abundances of the studied systems range from 12+log (O/H) = 8.29 ± 0.10 to 12+log (O/H) = 8.73 ± 0.04 (Table 5), clearly much larger than the expected values for galaxies with such a low stellar mass, which typically have 12 + log(O/H) $\leqslant$ 7.5 (see, e.g., Hidalgo 2017). This indicates that these systems have likely originated from gas stripped from larger galaxies, like SECCO 1 (see Pap-II for a deeper discussion).

The mean abundance and standard deviations reported in Table 5 are obtained from N2+03N2, hence they are limited to the few sources per system having estimates of O3N2. However, we can use the abundances from N2 (PP04 calibration), which are available for many more sources, to obtain a more realistic estimate of the uncertainties on the mean abundances and to study the chemical homogeneity of the various BCs. Unfortunately, the uncertainty on the abundance of individual sources can be quite large, ranging from 0.09 dex to 0.9 dex, providing poor constraints on the abundance spread, especially for BC1, where even the brightest sources have relatively low-S/N

Table 4
Metallicity of Individual Sources

Name	12+log(O/H) N2(PP04)	12+log(O/H) O3N2(PP04)	⟨ 12+log(O/H)⟩ N2+O3N2(PP04)	12+log(O/H) N2(M13)	12+log(O/H) O3N2(M13)	⟨ 12+log(O/H)⟩ N2+O3N2(M13)
BC1s11	8.28 ± 0.88	8.33 ± 1.02	8.31 ± 0.90	8.24 ± 0.88	8.27 ± 1.02	8.26 ± 0.89
BC1s12	8.27 ± 0.50	⋯	⋯	8.24 ± 0.50	⋯	⋯
BC1s13	8.23 ± 0.37	⋯	⋯	8.20 ± 0.37	⋯	⋯
BC1s14	8.39 ± 0.61	⋯	⋯	8.33 ± 0.61	⋯	⋯
BC1s15	8.20 ± 0.72	⋯	⋯	8.18 ± 0.72	⋯	⋯
BC1s20	8.23 ± 0.59	⋯	⋯	8.20 ± 0.59	⋯	⋯
BC1s80W	8.26 ± 0.56	8.50 ± 0.84	8.38 ± 0.60	8.23 ± 0.56	8.38 ± 0.84	8.30 ± 0.59
BC1s90W	8.12 ± 0.95	⋯	⋯	8.11 ± 0.95	⋯	⋯
BC1s92W	8.37 ± 0.90	⋯	⋯	8.31 ± 0.90	⋯	⋯
BC1s98W	8.17 ± 0.93	⋯	⋯	8.15 ± 0.93	⋯	⋯
BC3s4	8.09 ± 0.22	⋯	⋯	8.09 ± 0.22	⋯	⋯
BC3s9	8.12 ± 0.27	8.55 ± 0.47	8.34 ± 0.33	8.11 ± 0.27	8.42 ± 0.47	8.26 ± 0.32
BC3s10	8.13 ± 0.12	8.43 ± 0.16	8.28 ± 0.23	8.12 ± 0.12	8.34 ± 0.16	8.23 ± 0.20
BC3s13	8.19 ± 0.67	⋯	⋯	8.17 ± 0.67	⋯	⋯
BC3s15	8.06 ± 0.15	8.16 ± 0.18	8.11 ± 0.25	8.06 ± 0.15	8.16 ± 0.18	8.11 ± 0.23
BC3s16	8.28 ± 0.50	8.48 ± 0.71	8.38 ± 0.54	8.24 ± 0.50	8.37 ± 0.71	8.30 ± 0.52
BC3s18	8.07 ± 0.41	⋯	⋯	8.07 ± 0.41	⋯	⋯
BC3s19	8.19 ± 0.38	⋯	⋯	8.17 ± 0.38	⋯	⋯
BC3s26W	8.18 ± 0.64	8.44 ± 0.86	8.31 ± 0.67	8.16 ± 0.64	8.34 ± 0.86	8.25 ± 0.66
BC4s4L	8.65 ± 0.11	8.85 ± 0.40	8.75 ± 0.22	8.54 ± 0.11	8.61 ± 0.4	8.58 ± 0.20
BC4s8L	8.66 ± 0.09	8.70 ± 0.19	8.68 ± 0.22	8.54 ± 0.09	8.51 ± 0.19	8.53 ± 0.19
BC4s9L	8.64 ± 0.14	8.78 ± 0.42	8.71 ± 0.24	8.53 ± 0.14	8.57 ± 0.42	8.55 ± 0.22
BC4s10L	8.64 ± 0.1	8.97 ± 0.68	8.81 ± 0.22	8.53 ± 0.1	8.69 ± 0.68	8.61 ± 0.19
BC4s11L	8.74 ± 0.20	8.62 ± 0.34	8.68 ± 0.28	8.61 ± 0.20	8.46 ± 0.34	8.53 ± 0.26
BC4s12L	8.72 ± 0.16	8.75 ± 0.44	8.73 ± 0.26	8.60 ± 0.16	8.54 ± 0.44	8.57 ± 0.23
BC4s13L	8.79 ± 0.12	⋯	⋯	8.66 ± 0.12	⋯	⋯
BC4s14L	8.44 ± 0.63	⋯	⋯	8.37 ± 0.63	⋯	⋯
BC4s38WL	8.61 ± 0.12	⋯	⋯	8.51 ± 0.12	⋯	⋯
BC4s3L	8.60 ± 0.12	⋯	⋯	8.50 ± 0.12	⋯	⋯
BC4s15R	8.60 ± 0.17	⋯	⋯	8.50 ± 0.17	⋯	⋯
BC4s34WR	8.59 ± 0.12	⋯	⋯	8.49 ± 0.12	⋯	⋯
BC4s40WR	8.67 ± 0.12	⋯	⋯	8.56 ± 0.12	⋯	⋯
BC5s9	8.55 ± 0.13	8.78 ± 0.42	8.66 ± 0.24	8.46 ± 0.13	8.56 ± 0.42	8.51 ± 0.21
BC5s10	8.28 ± 0.38	⋯	⋯	8.24 ± 0.38	⋯	⋯
BC5s12	8.57 ± 0.09	8.87 ± 0.35	8.72 ± 0.22	8.48 ± 0.09	8.62 ± 0.35	8.55 ± 0.19

Note. Only abundance estimates with uncertainties <1.0 dex have been retained in this table. The individual uncertainties include also the uncertainty associated with the calibrating relations. $N_{\rm O/H}$: the number of sources used to compute the average oxygen abundance.

Table 5
Mean Properties of the Studied Targets

Name	R.A.$_{\rm J2000}$ (deg)	Decl.$_{\rm J2000}$ (deg)	$R_{\rm med}$ (arcsec)	$R_{\rm max}$ (arcsec)	F$_{int}$(Hα) (erg cm^{-2} s^{-1})	RV (km s^{-1})	$\sigma_{\rm RV}$ (km s^{-1})	$N_{\rm RV}$	⟨12 + log((O/H)⟩	$\sigma_{\rm (O/H)}$	$N_{\rm (O/H)}$
BC1	189.75754	12.20332	8.3	28.1	5.5E-16	1117	6	18	8.35	0.04(0.2)	2(10)
BC3	191.67637	10.36820	14.0	25.9	31.3E-16	1584	4	15	8.29	0.09(0.1)	5(9)
BC4L	186.60643	14.38645	8.9	38.1	18.9E-16	−70	16	10	8.73	0.04(0.05)	6(10)
BC4R	186.59117	14.39690	8.2	18.6	4.0E-16	−42	10	6	⋯	(0.08)	0(3)
BC4	186.60000	14.39000	33.5	56.1	23.0E-16	−60	20	16	8.73	0.04(0.04)	6(13)
BC5	186.62856	15.17447	5.0	40.8	5.7E-16	−74	6	4	8.70	0.03(0.08)	2(3)

Note. Coordinates: the median of the R.A. and decl. of the individual sources, except for BC4, where the position of the center has been estimated by eye. $R_{\rm med}$: the median angular distance from the center R. $R_{\rm max}$: the angular distance from the center of the outermost source. Flux$_{int}$(Hα): the total integrated observed Hα flux, from aperture photometry on continuum-subtracted Hα slices of the cubes. RV and $\sigma_{\rm RV}$: mean heliocentric RV and velocity dispersion. $N_{\rm RV}$: the number of sources used to obtain the median positions and mean velocities. ⟨12 + log(O/H)⟩ and $\sigma_{\rm O/H}$: average oxygen abundance and standard deviation. The adopted individual abundance values are the mean from the N2 and O3N2 indicators, according to the PP04 calibration. $N_{\rm O/H}$: the number of sources used to compute the average oxygen abundance. The numbers reported in parentheses for $\sigma_{\rm O/H}$ and $N_{\rm O/H}$ are the intrinsic dispersion, as computed with the maximum-likelihood algorithm (Section 4) and the number of sources involved in the estimate.

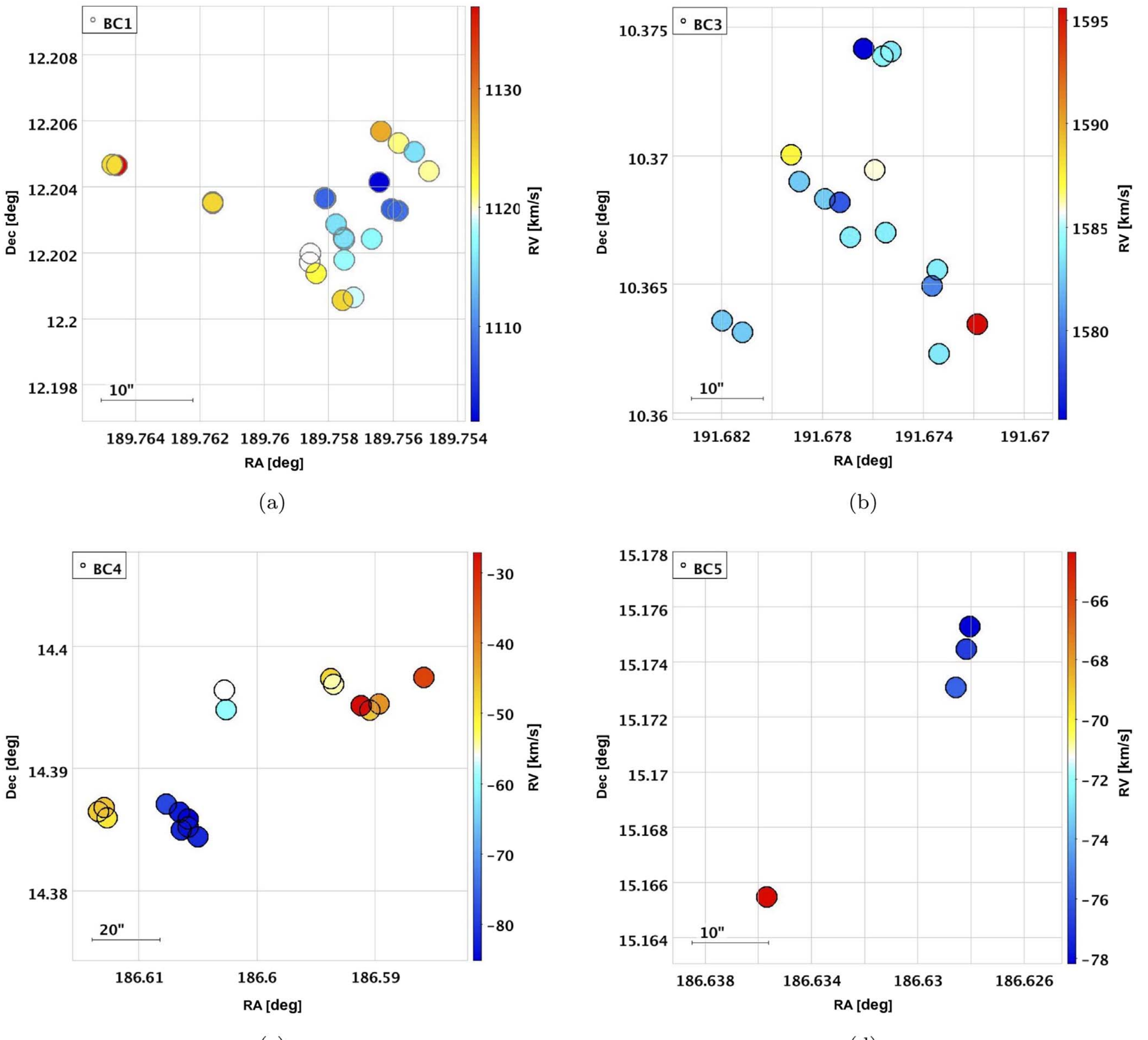

(a) (b)

(c) (d)

Figure 6. RV fields, in R.A. [deg] and decl. [deg], of the four systems, as traced by the individual H II sources. The BC4L and BC4R sources are shown on the same map. The source in the southeastern corner of panel (d) is BC5s3, which is not shown in Figure 2(c).

spectra. As in the case of the velocity dispersion, the metallicity dispersion is also not resolved by our data. However, we can attempt to obtain some collective constraints on the intrinsic dispersion.

Using the simple maximum-likelihood algorithm described by Mucciarelli et al. (2012), we find mean oxygen abundances of $\langle 12 + \log(\mathrm{O/H})\rangle = 8.3 \pm 0.2$, 8.2 ± 0.1, 8.66 ± 0.04, and 8.56 ± 0.07 for BC1, BC3, BC4, and BC5, respectively. In all cases, the most likely value for the intrinsic dispersion is zero, with the 1σ uncertainties ranging from 0.04 dex (BC4, from 13 sources) to 0.2 dex (BC1, from 10 sources). We conclude: (a) that the typical internal uncertainties for the mean abundances range from 0.04 dex to 0.2 dex; and (b) that all the systems appear to be remarkably homogeneous from the chemical point of view, again similar to SECCO 1. This supports the view that all the H II regions within a given BC were born from the same gas cloud. The fact that these sources were born together and now lie in clumps between ∼1 and 8 kpc (in projection) from each other may suggest that they are in the process of dissolving.

Finally, in Table 5, we also report the estimates of the total integrated Hα flux for each BC, obtained by photometry with large apertures on the continuum-subtracted images shown in Figure 1 and Figure 2. Once corrected for average extinction, using the extinction law of Calzetti et al. (2000), with $R_V = 3.1$, the integrated fluxes can be converted into estimates of the current star formation rate (SFR) using Equation (2) of Kennicutt (1998). The SFR for the considered systems ranges from

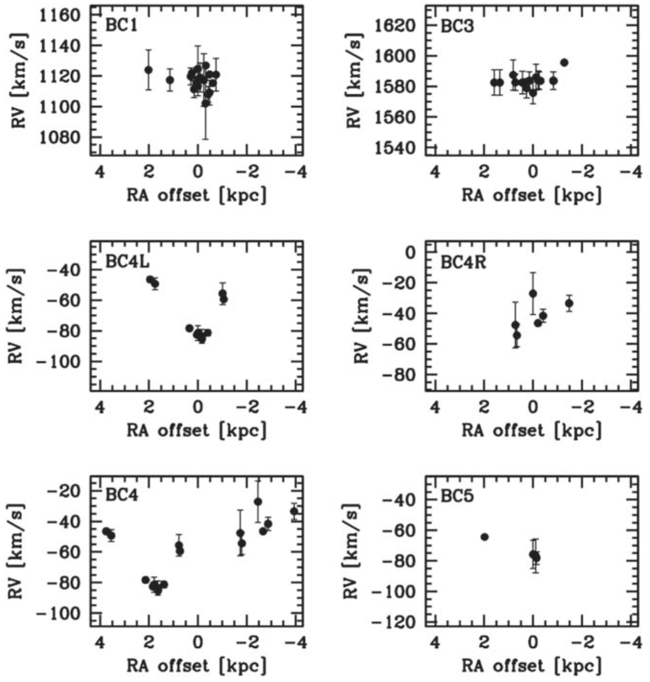

Figure 7. The projected distance from the center of the system along the R.A. direction (R.A. offset; east is toward the left) vs. RV for BC1, BC3, BC4L, BC4R, BC4 as a whole, and BC5, from left to right, top to bottom, respectively.

$\simeq 0.3 \times 10^{-3}\, M_\odot\, \mathrm{yr}^{-1}$ (BC1, BC5) to $\simeq 1.7 \times 10^{-3}\, M_\odot\, \mathrm{yr}^{-1}$ (BC3), to be compared with $\simeq 0.7 \times 10^{-3}\, M_\odot\, \mathrm{yr}^{-1}$ of SECCO 1, lying in the same range (Bellazzini et al. 2018).

5. Summary and Conclusions

We have presented the results of MUSE observations of five candidate isolated star-forming regions, optically selected to be similar to the prototype of the class SECCO 1. The acquired spectra allowed us to reject one of the candidates (BC2) and to confirm the other four (BC1, BC3, BC4, and BC5) as genuine star-forming regions, likely lying in the Virgo cluster of galaxies (see Pap-II for additional support for this conclusion). All the physical properties that we were able to measure are similar to those observed in SECCO 1. In particular:

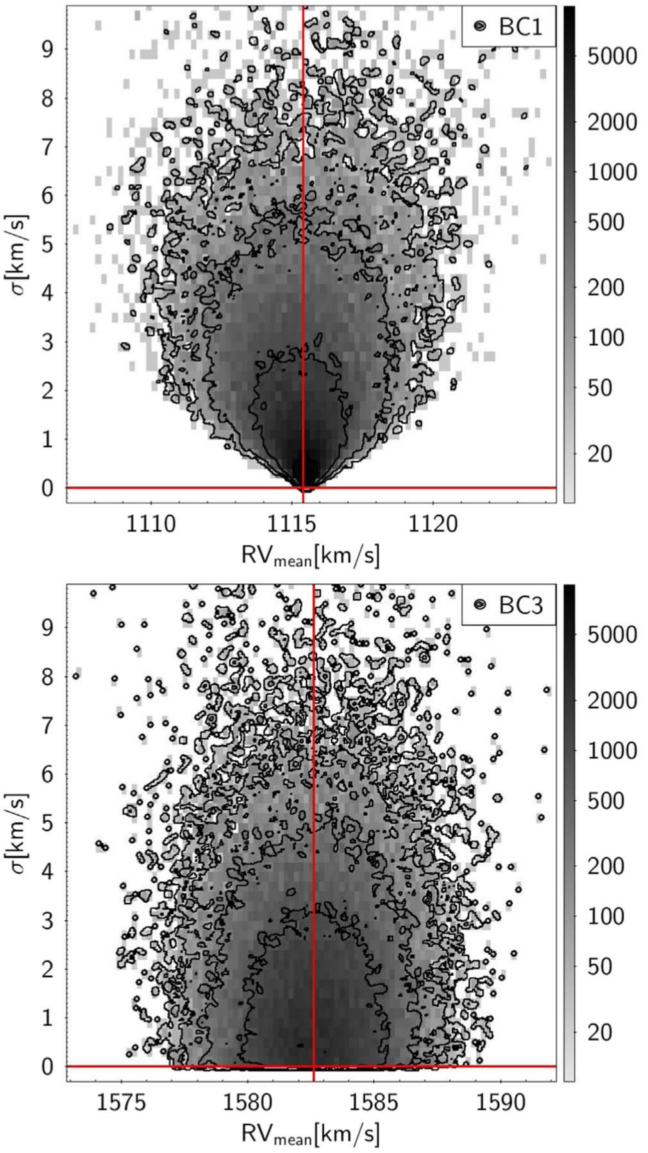

Figure 8. 2D posteriori PDFs of RV_{mean} and σ_{int}, as sampled with the MCMCs, for BC1 and BC3. The red vertical line marks the median of the RV_{mean} distribution, while the red horizontal line marks the mode of the σ_{int} distribution.

1. In all the confirmed BCs, we identified several H II regions, plus some diffuse hot gas.
2. The mean heliocentric velocity of each BC is consistent with membership in the Virgo cluster.
3. Each BC is typically composed of a few, separated, star-forming clumps, with systemic velocities within, at most, a few tens of $\mathrm{km\,s^{-1}}$. In the case of the most extended system, BC4, velocity gradients suggesting ongoing disruption are observed.
4. Our velocity estimates do not have sufficient precision to resolve the velocity dispersion of the considered systems, which, however, should be, in all cases, $\sigma \lesssim 20\,\mathrm{km\,s^{-1}}$. Still, given the available constraints, it seems unlikely that they can survive as gravitationally bound stellar systems.
5. The mean oxygen abundance of each BC is significantly larger than that expected for galaxies of similar stellar mass, strongly suggesting that they originated from gas clouds stripped from larger galaxies. Each BC appears to be internally homogeneous in terms of oxygen abundance, within the limits of the available observations, suggesting that all the associated sources were born from the same gas cloud.
6. The instantaneous SFR is $0.3 \times 10^{-3}\, M_\odot\, \mathrm{yr}^{-1} \lesssim \mathrm{SFR} \lesssim 2.0 \times 10^{-3}\, M_\odot\, \mathrm{yr}^{-1}$.

These results, together with those obtained from the HST and HI observations, are discussed in the companion paper, Pap-II, where an evolutionary path for the studied system is proposed.

We are grateful to an anonymous referee for useful comments and suggestions that improved the clarity of the paper. Based on observations collected at the European Southern Observatory under ESO program 0101.B-0376A. M.B. acknowledges the financial support of INAF—OAS Bologna, through the Ob. F. 1.05.01.01—Ricerca di Base funds. D.J.S. acknowledges support from NSF grants AST-1821967 and 1813708. A.K. acknowledges financial support from the State Agency for Research of the Spanish Ministry of Science, Innovation and Universities, through the "Center of Excellence Severo Ochoa" awarded to the Instituto de Astrofísica de Andalucía (SEV-2017-0709), and through the grant POSTDOC_21_00845, financed from budgetary program 54a Scientific Research and Innovation of the Economic Transformation, Industry, Knowledge and Universities Council of the Regional Government of Andalusia. E.A.K.A. is supported by the WISE research program, which is financed by the Dutch Research Council (NWO). R.R.M. gratefully acknowledges support from the ANID BASAL project FB210003. K.S. acknowledges support from the Natural Sciences and Engineering Research Council of Canada (NSERC). B.M.P. is supported by an NSF Astronomy and Astrophysics Postdoctoral Fellowship under award AST2001663. J.M.C., J.F., and J.L.I. are supported by NSF/AST grant 2009894. G.B. acknowledges support from the Agencia Estatal de Investigación del Ministerio de Ciencia en Innovación (AEI-MICIN) and the European Regional Development Fund (ERDF), under grants CEX2019-000920-S and PID2020-118778GB-I00/10.13039/501100011033.

Software: `Sextractor` (Bertin & Arnouts 1996), IRAF (Tody 1993), Topcat (Taylor 2005), SuperMongo (Lupton & Monger 1991), `R`, `JAGS`.

Facilities: VLT: Yepun (MUSE).

ORCID iDs

Michele Bellazzini https://orcid.org/0000-0001-8200-810X
Laura Magrini https://orcid.org/0000-0003-4486-6802
Michael G. Jones https://orcid.org/0000-0002-5434-4904
David J. Sand https://orcid.org/0000-0003-4102-380X
Giacomo Beccari https://orcid.org/0000-0002-3865-9906
Giovanni Cresci https://orcid.org/0000-0002-5281-1417
Kristine Spekkens https://orcid.org/0000-0002-0956-7949
Ananthan Karunakaran https://orcid.org/0000-0001-8855-3635
Elizabeth A. K. Adams https://orcid.org/0000-0002-9798-5111
Dennis Zaritsky https://orcid.org/0000-0002-5177-727X
Giuseppina Battaglia https://orcid.org/0000-0002-6551-4294
Anil Seth https://orcid.org/0000-0003-0248-5470
John M. Cannon https://orcid.org/0000-0002-1821-7019
Jackson Fuson https://orcid.org/0000-0002-8598-439X
John L. Inoue https://orcid.org/0000-0002-9724-8998
Burçin Mutlu-Pakdil https://orcid.org/0000-0001-9649-4815
Puragra Guhathakurta https://orcid.org/0000-0001-8867-4234
Ricardo R. Muñoz https://orcid.org/0000-0002-0810-5558
Paul Bennet https://orcid.org/0000-0001-8354-7279
Denija Crnojević https://orcid.org/0000-0002-1763-4128
Nelson Caldwell https://orcid.org/0000-0003-2352-3202
Jay Strader https://orcid.org/0000-0002-1468-9668
Elisa Toloba https://orcid.org/0000-0001-6443-5570

References

Adams, E. A. K., Giovanelli, R., & Haynes, M. P. 2013, ApJ, 768, 77
Adams, E. A. K., Cannon, J. M., Rhode, K. L., et al. 2015, A&A, 580, A134
Bacon, R., Vernet, J., Borisova, E., et al. 2014, Msngr, 157, 13
Beccari, G., Bellazzini, M., Battaglia, G., et al. 2016, A&A, 591, A56
Beccari, G., Bellazzini, M., Magrini, L., et al. 2017, MNRAS, 465, 2189
Bellazzini, M., Ibata, R. A., Martin, N., et al. 2019, MNRAS, 490, 2588
Bellazzini, M., Beccari, G., Battaglia, G., et al. 2015a, A&A, 575, A126
Bellazzini, M., Magrini, L., Mucciarelli, A., et al. 2015b, ApJL, 800, L15
Bellazzini, M., Armillotta, L., Perina, S., et al. 2018, MNRAS, 476, 4565
Bennet, P., Sand, D. J., Crnojević, D., et al. 2022, ApJ, 924, 98
Bertin, E., & Arnouts, S. 1996, A&AS, 117, 393
Boselli, A., Fossati, M., & Sun, M. 2022, A&ARv, 30, 3
Boselli, A., Voyer, E., Boissier, S., et al. 2014, A&A, 570, A69
Burkhart, B., & Loeb, A. 2016, ApJL, 824, L7
Calura, F., Bellazzini, M., & D'Ercole, A. 2020, MNRAS, 499, 5873
Calzetti, D., Armus, L., Bohlin, R. C., et al. 2000, ApJ, 533, 682
Cannon, J. M., Martinkus, C. P., Leisman, L., et al. 2015, AJ, 149, 72
Caplan, J., & Deharveng, L. 1986, A&A, 155, 297
Corbelli, E., Cresci, G., Mannucci, F., Thilker, D., & Venturi, G. 2021a, ApJL, 908, L39
Corbelli, E., Mannucci, F., Thilker, D., Cresci, G., & Venturi, G. 2021b, A&A, 651, A77
Fossati, M., Fumagalli, M., Boselli, A., et al. 2016, MNRAS, 455, 2028
Fumagalli, M., Fossati, M., Hau, G. K. T., et al. 2014, MNRAS, 445, 4335
Fumagalli, M., Gavazzi, G., Scaramella, R., & Franzetti, P. 2011, A&A, 528, A46
Gerhard, O., Arnaboldi, M., Freeman, K. C., & Okamura, S. 2002, ApJL, 580, L121
Giovanelli, R., Haynes, M. P., Adams, E. A. K., et al. 2013, AJ, 146, 15
Hidalgo, S. L. 2017, A&A, 606, A115
Jones, M. G., Sand, D. J., Bellazzini, M., et al. 2022a, ApJ, in press, arXiv:2205.01695 (Pap-II)
Jones, M. G., Sand, D. J., Bellazzini, M., et al. 2022b, ApJL, 926, L15
Junais, Boissier, S., Boselli, A., et al. 2021, A&A, 650, A99
Kapferer, W., Sluka, C., Schindler, S., Ferrari, C., & Ziegler, B. 2009, A&A, 499, 87
Kenney, J. D. P., Geha, M., Jáchym, P., et al. 2014, ApJ, 780, 119
Kennicutt, R. C. J. 1998, ARA&A, 36, 189
Kewley, L. J., Dopita, M. A., Sutherland, R. S., Heisler, C. A., & Trevena, J. 2001, ApJ, 556, 121
Kim, S., Rey, S.-C., Jerjen, H., et al. 2014, ApJS, 215, 22
Kniazev, A. Y., Pustilnik, S. A., & Zucker, D. B. 2008, MNRAS, 384, 1045
Lupton, R., & Monger, P. 1991, SuperMongo https://www.astro.princeton.edu/~rhl/sm/
Marino, R. A., Rosales-Ortega, F. F., Sánchez, S. F., et al. 2013, A&A, 559, A114
McQuinn, K. B. W., Skillman, E. D., Dolphin, A., et al. 2015, ApJ, 812, 158
Mei, S., Blakeslee, J. P., Côté, P., et al. 2007, ApJ, 655, 144
Mucciarelli, A., Bellazzini, M., Ibata, R., et al. 2012, MNRAS, 426, 2889
Nidever, D. L., Price-Whelan, A. M., Choi, Y., et al. 2019, ApJ, 887, 115
Osterbrock, D. E., & Ferland, G. J. 2006, Astrophysics of gaseous nebulae and active galactic nuclei (2nd edn.; Sausalito, CA: Univ. Science Books)
Pasha, I., Lokhorst, D., van Dokkum, P. G., et al. 2021, ApJL, 923, L21
Pettini, M., & Pagel, B. E. J. 2004, MNRAS, 348, L59
Poggianti, B. M., Gullieuszik, M., Tonnesen, S., et al. 2019, MNRAS, 482, 4466
Sand, D. J., Crnojević, D., Bennet, P., et al. 2015, ApJ, 806, 95
Sand, D. J., Seth, A. C., Crnojević, D., et al. 2017, ApJ, 843, 134
Saul, D. R., Peek, J. E. G., Grcevich, J., et al. 2012, ApJ, 758, 44
Taylor, M. B. 2005, in ASP Conf. Ser. 347, Astronomical Data Analysis Software and Systems XIV, ed. P. Shopbell, M. Britton, & R. Ebert (San Francisco, CA: ASP), 29
Tody, D. 1993, in ASP Conf. Ser. 52, Astronomical Data Analysis Software and Systems II, ed. R. J. Hanisch, R. J. V. Brissenden, & J. Barnes (San Francisco, CA: ASP), 173
Tollerud, E. J., Geha, M. C., Grcevich, J., Putman, M. E., & Stern, D. 2015, ApJL, 798, L21
Weilbacher, P. M., Streicher, O., Urrutia, T., et al. 2012, Proc. SPIE, 8451, 84510B
Yoshida, M., Yagi, M., Komiyama, Y., et al. 2012, ApJ, 749, 43